IEEE Access

Material Characterization and Radio Channel Modeling at D-Band Frequencies

BRECHT DE BEELDE[1], **DAVID PLETS**[1], (Member, IEEE), **CLAUDE DESSET**[2], (Member, IEEE), **EMMERIC TANGHE**[1], (Member, IEEE), **ANDRÉ BOURDOUX**[2], (Senior Member, IEEE), **AND WOUT JOSEPH**[1], (Senior Member, IEEE)

[1]Department of Information Technology, Ghent University/IMEC, 9052 Ghent, Belgium
[2]IMEC, 3001 Leuven, Belgium

Corresponding author: Brecht De Beelde (brecht.debeelde@ugent.be)

ABSTRACT As the throughput requirements for wireless communication links keep rising, characterization of sub-THz radio channels is necessary. This paper presents the results of a radio channel measurement campaign in which we characterize the full D-band, ranging from 110 to 170 GHz, for distances up to 5 m. We measured penetration and reflection loss for a broad set of materials that are commonly used in indoor environments, including wood, glass, acrylic, and concrete, and measured corner diffraction losses. Measurements over the full 60 GHz bandwidth reveal frequency selectivity as well as a periodic variation of both penetration and reflection loss, which is attributed to the thin film effect. Based on measurements in a conference room and outdoors, we create a spatio-temporal channel model for the conference room and an outdoor path loss model. The channel models show that the radio channel is extremely sparse to multipath components, containing only a Line-of-Sight path with signal attenuation close to path loss in free space, and first-order reflections with a measured attenuation that corresponds to the sum of the path and reflection loss.

INDEX TERMS Channel characterization, D-band, diffraction, millimeter wave propagation, modeling, path loss, penetration, reflection, sub-THz.

I. INTRODUCTION

In the last decade, research on wireless communication at mm-wave frequencies up to 100 GHz made fifth generation (5G) communication possible [1]–[7]. Nevertheless, exploration of a new radio spectrum is needed to enable beyond 5G applications, requiring high-throughput wireless connectivity. Some of these future high-capacity applications, such as wireless backhaul and fixed wireless access, require long-range wireless communication, whereas other applications require high data rates at lower distances. Examples of the latter include close proximity data kiosks, augmented and virtual reality (AR/VR), and holographic displays. Sub-THz communication is considered a key technology for sixth generation (6G) applications [8], [9]. In the D-band, ranging from 110 to 170 GHz, enough bandwidth is available, and this frequency range is apt for short-range high-throughput communication.

Channel characterization at D-band frequencies is ongoing, but more research is needed to obtain a unified D-band channel model, as existing channel models consider only a sub-band around the center frequency 140 GHz, or use small antenna separations. Cheng *et al.* performed Line-of-Sight (LOS) path loss (PL) measurements up to 0.86 m and compare 30 GHz, 140 GHz, and 300 GHz frequency bands [10], concluding that measured PL is close to free space path loss (FSPL) for all three frequency bands, with frequency-dependent fluctuations caused by the environment or reflections on the measurement equipment. Path loss, spatial and temporal characteristics at 140 GHz and 28 GHz are compared by Nguyen *et al.* for a shopping mall environment [11]. They confirmed the sparsity of the 140 GHz channel and found a high spatial correlation between the channels corresponding to the two frequencies. Pometcu *et al.* use a vector network analyzer (VNA) based channel sounder with a larger bandwidth of 30 GHz to characterize LOS and non-Line-of-Sight (NLOS) radio propagation in a laboratory setting and NLOS propagation in an office environment [12], [13], reporting a PL exponent below 2 for a LOS channel,

The associate editor coordinating the review of this manuscript and approving it for publication was Matti Hämäläinen.

and body and wall attenuation up to 27 dB. Kim *et al.* consider the full D-band channel [14], proposing a D-band PL model for LOS, obstructed LOS, and reflected NLOS communication for a distance up to 90 cm. Al-Saman *et al.* performed channel measurements at frequency 108 GHz in an industrial environment and with antenna separations up to 5 m, reporting PL exponents ranging from 1.6 to 2 [15]. Dupleich *et al.* created spatio-temporal channel models for a conference room at 190 GHz, using a channel sounder with a bandwidth of 7.5 GHz [16]. Diffraction is well-studied at mm-wave frequencies [17]–[19] but not yet at sub-THz frequencies.

As channel modeling via ray-tracing has proven to be an alternative for stochastic channel models at mm-wave frequencies and beyond [20]–[25], propagation characteristics of different materials should be investigated. Piesiewicz *et al.* provide the refractive index and absorption coefficients for frequencies up to 350 GHz for plaster, glass, wood, and wallpaper via time-domain spectroscopy [26]–[28]. Correia and Frances estimate material characteristics based on power measurements at frequency 60 GHz [29], and several papers present penetration and reflection loss measurements, but it is clear that for a lot of materials the propagation characteristics above 100 GHz are not yet known [30]. Penetration loss is the attenuation when a signal penetrates through a blocking material and is well-studied at mm-wave frequencies [17], [31]–[33]. Xing *et al.* provide guidelines for measuring penetration loss [34] and present penetration and reflection loss measurements using a 140 GHz channel sounder with a 4 GHz bandwidth for common materials such as drywall and glass [35]. Reflection, transmission, and scattering measurements are studied for the same set of materials [36]. Penetration through a plasterboard wall and a door is investigated by Pometcu [12]. Penetration and reflection losses for an incident angle of 45° are provided by Olsson *et al.* using a VNA-based channel sounder with a bandwidth of 7 GHz and a center frequency of 140 GHz [37]. Kim *et al.* reported that the measured PL for the reflected NLOS case is close to FSPL when the reflector is an aluminum plate and the incident angle equals the reflection angle [14].

We have designed a VNA-based D-band channel sounder with a 60 GHz bandwidth for characterizing the full D-band radio channel for distances up to 5 m. The goal of this paper is to fill existing research gaps on D-band propagation channels. In particular, we present reflection and penetration loss measurements for a broad set of materials commonly used in indoor environments, and fit the refractive index to the measurement data. The results of these reflection and penetration measurements can be used in ray-tracing applications. Furthermore, we present indoor and outdoor propagation measurements to create a D-band channel model that can be used for network performance evaluation. To the best of the authors' knowledge, this is the first paper presenting reflection and penetration loss measurements in the D-band for different materials such as acrylic and tabletop wood, as well as presenting corner diffraction
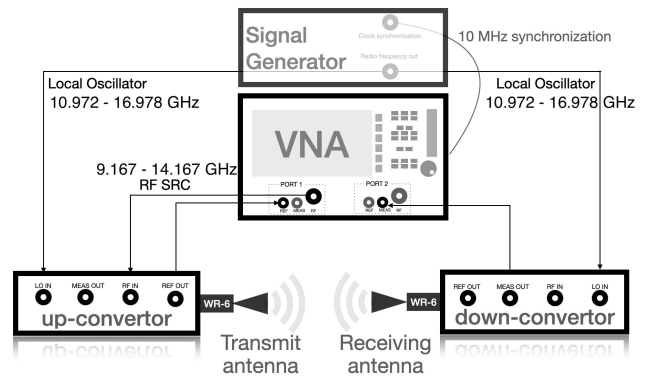
FIGURE 1. Channel sounder schematic overview. A vector network analyzer (VNA) creates a radio frequency source (RF SRC) at port 1, which is up-converted via frequency multiplication and down-converted using a local oscillator (LO) signal generated by an external signal generator. The down-converted reference and measurements signals are analyzed by the VNA.

and both indoor and outdoor channel models valid for the full 60 GHz bandwidth.

The paper is structured as follows. Section II presents the methodology, including the channel sounder design and measurement setups. The results are presented in Section III and the conclusions follow in Section IV.

II. METHODOLOGY
A. CHANNEL SOUNDER DESIGN
A schematic overview of the channel sounder setup is presented in Fig. 1. A two-port VNA generates a radio frequency (RF) source input from 9.167 to 14.167 GHz that is multiplied by a factor 12 via frequency multiplication using an external frequency up-converter, which results in an RF output in the frequency range 110 to 170 GHz. The frequency converter contains a harmonic mixer for down-conversion, which is used to generate the reference signal measured by the VNA. The harmonic mixer has a multiplication factor 10 and uses a 10.972 to 16.9782 GHz local oscillator (LO) input that comes from an external signal generator. At the receiver side, the obtained signal is down-converted using the harmonic mixer of the frequency down-converter that uses the same LO input, and the down-converted signal is sent to the measurement port of the VNA. The VNA measures the phase and amplitude difference between the reference signal at port 1 and the measured signal at port 2.

Standard gain pyramidal horn antennas with a gain increasing from 22.2 dBi for 110 GHz to 23.3 dBi for 170 GHz are used as transmit (TX) and receive (RX) antennas and are connected to the frequency converters' WR-6 waveguides. The antennas have a H-plane half power beam width (HPBW) ranging from 13.2° for 110 GHz to 12° for 170 GHz and an E-plane HPBW ranging from 12° for 110 GHz to 8.8° for 170 GHz. The Fraunhofer far-field distance d_F of these antennas, calculated via (1), equals 0.55 m at 170 GHz as D is equal to 0.022 m and the wavelength λ is 0.00176 m.

$$d_F = \frac{2D^2}{\lambda} \qquad (1)$$

TABLE 1. D-band channel sounder parameters.

Parameter	Value
Start frequency	110 GHz
Stop frequency	170 GHz
Number of frequency points	3001
Transmit power	16 dBm
Dynamic range	95 dB
Distance range	0.5 - 5 m
Measurement bandwidth	100 Hz

Using 3001 frequency points, the frequency step size is 20 MHz. The intermediate frequency (IF) measurement bandwidth (BW) of the VNA is set to 100 Hz and the output power of the signal generator is set to 16 dBm. A normalized forward calibration is performed before all measurements, with the converters' WR-6 waveguides as the reference plane of the calibration. No averaging is performed on the VNA. The cables connecting the signal generator, VNA, and converters are characterized for signal attenuation and group delay. The group delay of the cables carrying the LO signal is less than 100 ps and the attenuation at 17 GHz is less than 10 dB.

From the measured transfer function $H(f)$, we get PL via (2), with N the number of frequency sweeps for the considered scenario, $G_a(f)$ the frequency-dependent antenna gain and $C(f)$ a correction term based on reference measurements that are performed in the center of the lab, without nearby reflectors [38].

$$\text{PL}_{\text{dB}}(f) = -10\log_{10}\left(\frac{1}{N}\sum_{i=1}^{N}|H_i(f)|^2\right) + 2G_a(f) + C(f)$$
(2)

The inverse discrete Fourier transformation (IDFT) results in the channel impulse response (CIR) from which the averaged power delay profile (PDP) is found, as can be seen in (3), with $\mathcal{W}$ the Hann window.

$$\text{PDP}(k\Delta\tau) = \frac{1}{N}\sum_{i=1}^{N}|\text{IDFT}(\mathcal{W}(f)\cdot H_i(f))|^2$$
(3)

Table 1 summarizes the key channel sounder properties and characteristics. The IF BW of 100 Hz and 16 dBm transmit power results in a dynamic range of the sounder of 95 dB. The VNA's sweep time is 45 s during which the channel is assumed to be static, as no people were present during the measurements. Due to the high bandwidth, we obtain a high temporal resolution $\Delta\tau$ of 0.0167 ns. The maximum resolvable time delay of 50 ns corresponds to a path length of 15 m. The maximum distance between the TX and RX antennas is limited by the cable length of 10 m. The validation of the channel sounder is presented in previous work [38].

B. PENETRATION AND REFLECTION LOSS CHARACTERIZATION

For radio channel characterization via ray-tracing it is of utmost importance to have accurate reflection and penetration loss data for different materials. Therefore, we characterized reflection and penetration loss for the materials listed in Table 2. These materials are selected as they are assumed to be used in the most common objects present in indoor environments.

For the penetration and reflection loss measurements, both antennas are at the same height of 1.3 m above the ground and leveled horizontally. The height of the antenna, in combination with the antenna's narrow HPBW, ensures that no ground or ceiling reflections are received. A laser pointer is used for the antenna alignment. For each measurement scenario, 5 co-polarized vertical (VV) and horizontal (HH) measurements are performed with a 1 mm distance variation, in order to spatially average over the small scale fading (SSF) area. At the mid-band frequency 140 GHz, 1 mm corresponds to approximately half a wavelength. The 1 mm distance variations cause FSPL variations less than 0.01 dB. We obtain averaged measured PL via (2), with $C(f)$ the frequency-dependent correction factor that is obtained from a reference measurement with antenna separation 2 or 3 m and without any material under test (MUT) obstructing the LOS path.

1) PENETRATION LOSS

We performed measurements with a distance of 2 m as well as a distance of 3 m between the antennas. For both distances, the MUT is placed right in the middle between the two antennas. The material dimensions are large enough to ensure that no diffraction occurs and all received power has penetrated the MUT. Due to the narrow HPBW of the used antennas and the absence of objects nearby the measurement setup, no environmental reflections are received. This is confirmed by an analysis of the PDP, which only shows one peak. Subtracting theoretic FSPL from the measured PL (corrected based on the reference measurement) results in measured penetration loss as a function of frequency. Dividing the attenuation (in dB) by the thickness of the measured material results in penetration loss as a function of frequency and thickness.

A second processing approach is also considered and yields similar results. In this approach, we first split up the 60 GHz frequency band into 10 GHz sub-bands. For every subband, we get the PDP via (3). One sub-band contains 500 frequency points, which results in a time-domain resolution of 0.10 ns. The penetration loss is then obtained by subtracting the power in the (only) peak of the PDP from the power in the peak of the reference LOS measurement with the same distance.

2) REFLECTION LOSS

For the reflection measurements, the TX and RX antennas point towards a reflection point on the MUT with an angle varying from 15° to 60° with respect to the surface normal in the reflection point. The distance from the antennas to the material ranges from 1 m to 1.5 m. We performed co-polarized VV and HH measurements for every material, angle, and polarization setup. Similarly to the penetration loss measurements, we define reflection loss as the added

TABLE 2. Material thickness and dimensions for penetration and reflection loss measurements.

Material	Thickness	Dimensions
Medium-density fibreboard (MDF) wood	18 mm	122x244 cm
Tabletop of laminated wood with veneer top layer	25.4 mm	120x82 cm
Polyvinyl chloride (PVC)	10 mm	180x100 cm
Acrylic/plexiglass (Altuglas PMMA)	3 mm	150x125 cm
Cardboard	5 mm	60x90 cm
Glass	22 mm	60x240 cm
Stainless steel	1.5 mm	30x60 cm
Concrete	45 mm	variable
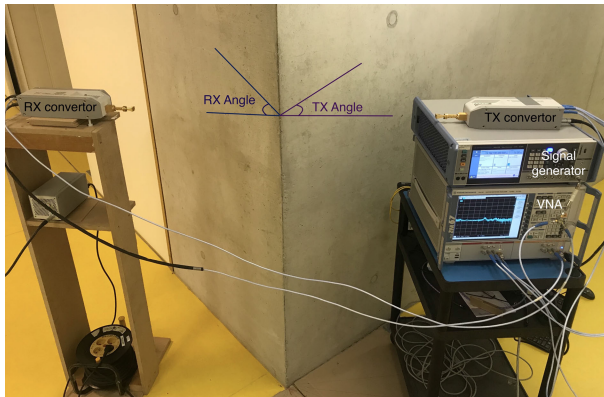
FIGURE 2. Diffraction measurement setup, with both antennas placed at 50 cm from the corner, TX angle 37° and RX angle 45°.

FIGURE 3. Conference room measuring 4 m by 4.6 m with a distance of 3.75 m between the TX antenna (on the left) and the RX antenna (on the right) placed on a turntable. Two walls are made of layered drywall, the wall on the back is made of wood and the wall on the left (not visible on the picture) is made of glass.
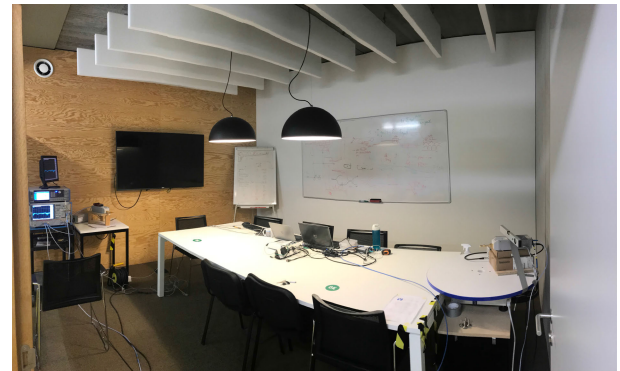
loss compared to the FSPL corresponding to the distance equal to the reflected path length. Based on the reflection loss measurements, the refractive index of the different materials is estimated via a minimum mean squared error (MMSE) estimation of (4). In this equation, θ is the incident angle, n is the refractive index of the MUT and r is the reflection coefficient for the perpendicular polarization, which is obtained from the co-polarized VV reflection loss measurements.

$$r = \frac{\cos(\theta) - \sqrt{n^2 - \sin^2(\theta)}}{\cos(\theta) + \sqrt{n^2 - \sin^2(\theta)}} \quad (4)$$

The antenna cross-polarization discrimination is measured via the methodology outlined by Xing *et al.* [34] and found to be 21.7 dB. For an incident angle of 30°, cross-polarized measurements with a vertically polarized TX antenna and horizontally polarized RX antenna are performed.

C. CORNER DIFFRACTION
Next to penetration and reflection, diffraction is another propagation mechanism that needs to be considered for NLOS communication. We performed co-polarized VV diffraction measurements around a 90° concrete corner of a corridor. Figure 2 shows a picture of the measurement setup. Both antennas are placed at the same height of 1.3 m above ground level at 0.5 m from the corner, with the angle between the antennas and the wall ranging from 45 to 22°. Multiple measurements are performed and averaged for every TX-RX angle combination. We obtain diffraction loss as a function of frequency by subtracting FSPL corresponding to a distance of 1 m from the measured PL which we derive via (2).

## D. SPATIO-TEMPORAL CONFERENCE ROOM CHANNEL MODEL
We performed angular measurements for two separations, 2.6 m and 3.75 m, in a conference room measuring 4 m by 4.6 m of which a picture is shown in Fig. 3. One wall is made of glass, another is made of wood and the remaining two walls are made of layered drywall. Both antennas are vertically polarized, placed at the same height of 0.8 m, and rotated around the antenna aperture in steps of 12°, which corresponds to the antennas' HPBW at 140 GHz. We measure physical received power for every TX and RX angle, which results in a power angular profile (PAP) from which we get angle of arrival (AoA) and angle of departure (AoD) information with an angular resolution of 12° by integration over all TX and RX angles, respectively. For every TX and RX angle combination, we obtain the power delay profile (PDP) by performing an inverse discrete Fourier transform after applying a Hann window. This results in a spatio-temporal model with received power as a function of delay and AoA by integrating the PDPs over all TX angles. From the PDPs and PAPs, root-mean-square (RMS) delay and angular spread values are obtained.

E. OUTDOOR PATH LOSS MODEL
We performed outdoor LOS PL measurements for distances ranging from 0.8 to 5.0 m in steps of 0.1 m. Both antennas are at the same height of 1.3 m above ground level, and the TX antenna is pulled away from RX antenna along two tracks that

(a) Track 1, parallel to window, distance 4.4 m
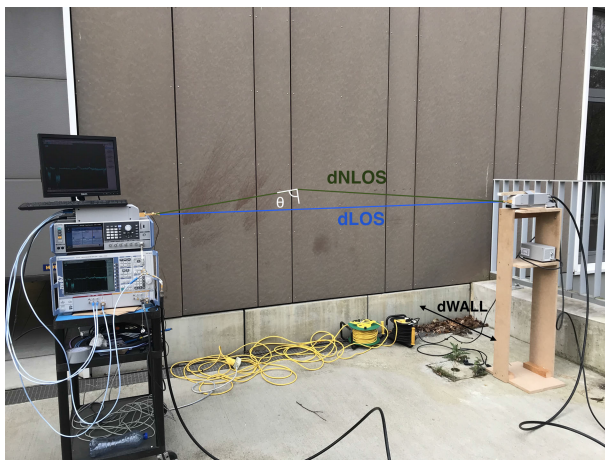
(b) Track 2, parallel to wall, distance 2.3 m

FIGURE 4. Two outdoor measurement tracks, parallel to building, with a Line-of-Sight path and a non-Line-of-Sight path via reflection on the building facade.

are both parallel to a building and shown in Fig. 4. Track 1 is next to the building's window whereas track 2 is next to the wall. The distance from the measurement track to the building is 1.2 m. Both antennas are leveled and are aligned to each other using a laser.

The measurement data is averaged over 1 GHz subbands and fitted to the PL model from (5), with d the distance in meter between the antennas, PL_0 the reference PL in dB at 1 m, n the PL exponent and χ the shadow fading term based on a zero-mean normal distribution with standard deviation σ. We considered both a close-in (CI) model for which the reference PL is calculated via Friis formula and the PL exponent is the only regression parameter, as well as a floating-intercept (FI) PL model for which both the reference PL and PL exponent are fitted to the measurement data.

$$PL_{dB}(d, f) = PL_0(f) + 10\, n(f)\log_{10}(d/1\text{m}) + \chi \quad (5)$$

In addition to LOS measurements, we also define the attenuation of the best NLOS path by measuring PL corresponding to the reflected path for distances ranging from 1.5 to 5.0 m

in steps of 0.5 m. For track 1, the signal reflects on glass whereas for track 2, it reflects on the building facade. At every distance, we perform 3 measurements with a slight difference in reflection angle. We compare the averaged measured attenuation of the reflected path to geometry-based calculations. The distance of the NLOS path is calculated via (6), with d_{wall} the distance to the wall and d_{LOS} the LOS distance between TX and RX. The incident angle is calculated via (7).

$$d_{\text{NLOS}} = 2\sqrt{\left(\frac{d_{\text{LOS}}}{2}\right)^2 + d_{\text{wall}}^2} \quad (6)$$

$$\theta = \frac{\pi}{2} - \text{atan}\left(\frac{2\, d_{\text{wall}}}{d_{\text{LOS}}}\right) \quad (7)$$

III. RESULTS

A. PENETRATION LOSS

Table 3 lists the measured penetration loss values for different frequencies, materials, and polarizations, averaged over 10 GHz subbands and over the two measurement distances. The median difference between the results of measurements with 2 and 3 m distance is 0.2 dB and a maximum difference of 2.1 dB occurs for the horizontally polarized measurements of MDF wood above 160 GHz. This confirms the accuracy and methodology of the measurement. Penetration loss as a function of frequency and per cm thickness is shown in Fig. 5 for the different materials from Section II-B except stainless steel and the concrete slab. For these materials, we could not measure the penetration loss as the measurement was within the noise floor of the channel sounder. Given the distance between the TX and RX antennas and the maximum measurable PL of 135 dB, the penetration loss is higher than 50 dB. Both the time-domain and frequency-domain analysis give the same penetration loss results.

For acrylic and PVC we see a periodic behavior that is caused by multipath propagation and confirmed by a thin film analysis. We consider the generalized scenario from Fig. 6 where the incident plane wave is not perpendicular to the surface of the MUT. An incoming plane wave hits the MUT at incident angle θ. The reflected plane wave has a 180° phase shift as the dielectric constant of the MUT is assumed to be higher than that from air. Using the same assumption, no phase shift occurs at the reflection within the MUT. There is positive interference when the length of the reflected path inside the MUT is an integer multiple of the wavelength, but as the permittivity inside the MUT differs from free space, the wavelength is shortened. The wavelength within the MUT is $\lambda_{\text{air}}/n_{\text{MUT}}$. Therefore, the condition for constructive interference is given by (8), with m an integer value, n_{MUT} the refractive index of the MUT, λ_{air} the wavelength in the air, t the thickness of the MUT and ϕ the angle with respect to the normal within the MUT, which relates to the incident angle θ via Snell's law.

$$2\, t\, \cos(\phi) = m\, \frac{\lambda_{\text{air}}}{n_{\text{MUT}}} \quad (8)$$

Based on (8) we can calculate the frequency offset in between two frequencies for which constructive interference

TABLE 3. Averaged measured penetration loss [dB] for different materials and frequencies, for both vertical (VV) and horizontal (HH) co-polarizations.

Material	Polarization	115 GHz	125 GHz	135 GHz	145 GHz	155 GHz	165 GHz
Wood	VV	10.7	11.2	12.2	13.6	15.2	16.7
Wood	HH	11.4	12.2	13.6	15.1	16.6	17.9
Tabletop	VV	30.0	33.3	37.4	35.8	42.1	50.5
Tabletop	HH	31.2	33.9	34.8	38.2	43.1	44.5
PVC	VV	2.6	2.9	3.1	3.5	3.8	4.2
PVC	HH	2.6	2.8	3.2	3.4	3.7	4.1
Acrylic	VV	1.3	0.8	1.0	1.5	1.1	1.1
Acrylic	HH	1.3	0.9	0.8	1.4	1.2	0.9
Cardboard	VV	2.7	3.5	3.7	3.0	3.7	3.3
Cardboard	HH	2.4	3.2	3.7	2.8	2.8	2.9
Glass	VV	18.4	20.3	21.7	24.1	26.2	28.2
Glass	HH	18.1	20.0	21.2	23.8	25.9	27.9
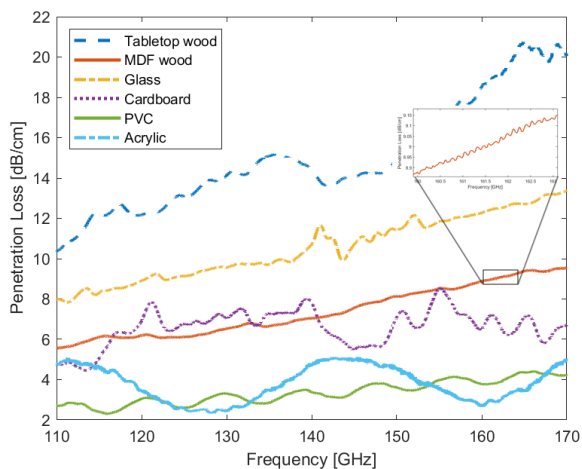
(a) Vertical polarization (VV)
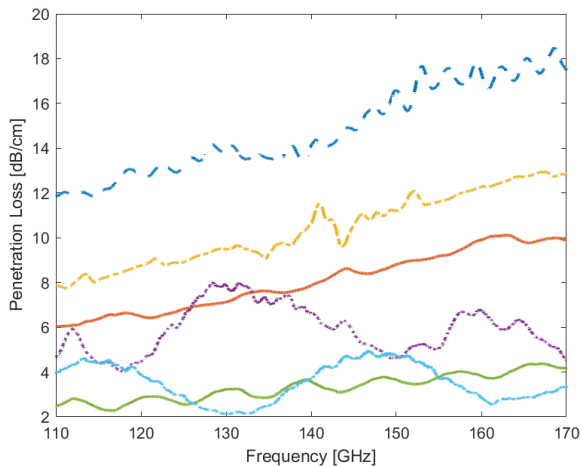
(b) Horizontal polarization (HH)

FIGURE 5. Penetration loss as a function of frequency per cm thickness for the different materials.

occurs via (9), given a fixed thickness t and known refractive index n_{MUT}.

$$\Delta f = f_{m+1} - f_m = \frac{c}{2\, t\, n_{MUT}\, \cos(\phi)} \quad (9)$$

In our measurements, the incident angle θ and therefore also ϕ is zero. Based on (9) and the frequency interspacing

from Fig. 5 we calculate the refractive index n_{MUT}. The averaged frequency offset, also called the free spectral range, for PVC is 9 GHz, which corresponds to a n_{MUT} of 1.66. As a validation, we use this refractive index to find the minimum penetration loss values, corresponding to constructive interference, and the maximum penetration loss values, corresponding to destructive interference, via (10). For m ranging from 13 to 17 the maxima and minima of the penetration loss measurements correspond to the calculated frequency.

$$f_{constructive} = m \cdot \frac{c}{2\, t\, n_{MUT}}$$
$$f_{destructive} = (m - 0.5) \cdot \frac{c}{2\, t\, n_{MUT}} \quad (10)$$

The free spectral range for acrylic is 32 GHz, corresponding to a refractive index n_{MUT} of 1.557 as the thickness of the acrylic sheet is 3 mm. Using (10) we get constructive interference for frequencies 128 and 160 GHz and destructive interference for 112 and 144 GHz, which corresponds to the minima and maxima in Figure 5. It should be noted that even though the periodic behavior is visible for acrylic and PVC, it is also present for the other materials. The thicker the material, the smaller the free spectral range. For MDF with a thickness of 18 mm the spectral range becomes so small that the frequency variation is not visible due to the averaging. This is illustrated in the zoomed region of Fig. 5a which shows the penetration loss of MDF wood per cm thickness. The variation in penetration loss for cardboard is caused by the irregular internal structure of the cardboard, i.e., two layers with a third one woven in between.

From Fig. 5, we conclude that there is no significant dependency on polarization, compared to findings in the 30-50 GHz mm-wave frequency band [17] where an additional attenuation up to 2 dB/cm is reported dependent on the polarization. For MDF, tabletop, PVC, and glass there is a linear relationship with frequency. Therefore, we fit the averaged penetration losses per cm thickness to the linear model of (11), with $L_{110\,GHz}$ the penetration loss in dB at 110 GHz, f the frequency in GHz, F the frequency-dependent term and t the material thickness in cm. Table 4 contains the values for $L_{110\,GHz}$ and F for the different materials.

$$L_{penetration}(f, t) = t \cdot (L_{110\,GHz} + (f - 110) \cdot F) \quad (11)$$

TABLE 4. Fitted frequency dependent penetration loss for the different materials per cm thickness.

| Parameter	MDF	Tabletop	PVC	Acrylic	Cardboard	Glass	Steel	Concrete
$L_{110\,\text{GHz}}$ [dB]	5.7	11.3	2.4	3.7	5.9	5.7	> 300	> 10
F [dB/GHz]	0.07	0.12	0.03	0	0	0.07	-	-
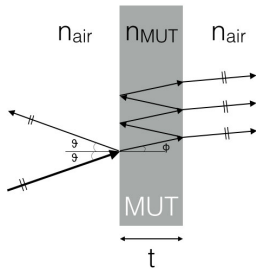
FIGURE 6. Schematic overview of penetration measurement through a thin material under test (MUT) resulting in a periodic pattern due to constructive and destructive interference.

(a) Vertical polarization (VV)

(b) Horizontal polarization (HH)

FIGURE 7. Reflection loss as a function of frequency for the different materials at incident angle 30°.

With a loss of 5.7 dB/cm at 110 GHz, penetration loss for wood is higher in the D-band compared to mm-wave frequencies, e.g., the penetration loss ranges from 2.4 dB/cm to 4.2 dB/cm at 45 GHz [17] and the penetration loss of a wooden door is 4.6 dB/cm at 73 GHz [32]. Compared to these measurements, the absorption coefficient of 1.7 dB/cm reported in [26] seems to be rather low. Comparing our measurement results to time-domain spectroscopy, the measured penetration loss of acrylic is slightly higher than the reported loss of 2.1 dB/cm [28]. The measured penetration loss of glass is 5.7 dB/cm at 110 GHz which is higher than the loss of 4.1 dB/cm from [28], but 3 dB lower than the D-band measurements performed in [35]. Our measured penetration loss of glass is similar to other measurements that were performed at 73 GHz [32]. From this, we conclude that there is a large variation in penetration loss of glass, which we believe largely depends on the composition and structure of the glass panel, e.g., whether it is coated glass, safety glass, or regular glass. The penetration loss of cardboard is in line with literature [37].
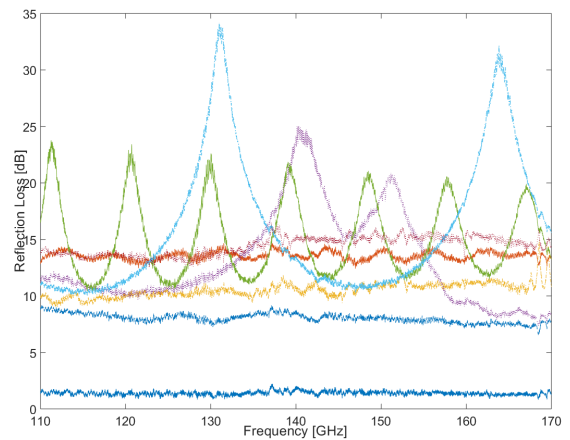
B. REFLECTION LOSS

Figure 7 shows the measured reflection loss as a function of frequency for the different polarizations for a fixed incident angle of 30° with respect to a line normal to the MUT. Similar to the penetration loss measurements, we see a periodic behavior for both PVC, and acrylic, with the same frequency offset of 9 GHz for PVC, and 32 GHz for acrylic. In contrast with the penetration loss, there is no clear dependence of reflection loss with frequency. The median reflection loss values for the different materials, angles and polarizations are presented in Table 5.

For incident angles up to 45° there is a trend that the reflection loss decreases with increasing angle, which is in line with the Fresnel reflection coefficients. As expected, the lowest reflection loss is measured for stainless steel (1.2 dB),
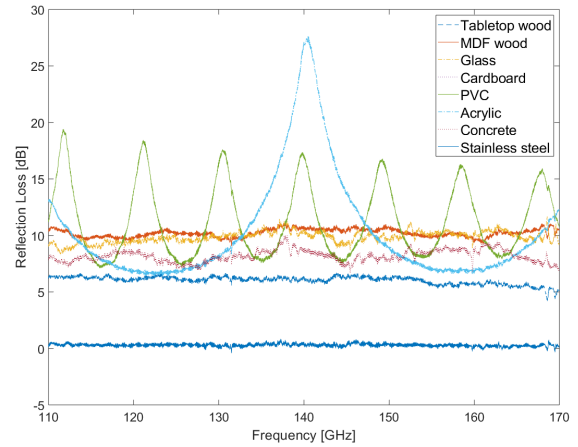
followed by the wooden tabletop (4.3 dB), which has the highest measurable penetration loss. As acrylic and PVC have lower penetration losses, it follows that they have a higher reflection loss (respectively 8.1 and 8.5 dB). Similar to the penetration loss measurements, there is a periodic variation for acrylic and PVC which is attributed to the constructive and destructive interference of multipath propagation within the medium. The higher reflection losses for horizontal co-polarized measurements compared to vertical co-polarized measurements are expected as for the VV measurements the MUT is parallel to the plane of incidence.

The reflection loss for drywall reported in [36] is 7.5 dB at 30°, which is similar to a tabletop material, lower than

TABLE 5. Median reflection loss [dB] for different materials, angles and polarizations, with estimated refractive index.

| angle material	15°		30°		45°		60°		estimated refractive index
	VV	HH	VV	HH	VV	HH	VV	HH	
Wood	11.8	13.6	10.2	13.6	8.8	15.8	10.9	27.3	1.51
Tabletop	6.2	7.2	6.0	8.0	4.3	8.9	7.7	13.9	2.40
PVC	11.4	11.5	10.4	14.2	8.5	16.0	10.9	29.7	1.53
Acrylic	11.5	12.1	8.5	13.6	8.1	15.3	11.5	33.5	1.58
Cardboard	21.8	10.2	20.3	11.6	5.8	13.6	14.8	26.7	1.28
Glass	7.6	11.4	9.9	10.5	7.8	8.5	1.6	12.5	2.25
Stainless steel	1.4	1.5	0.3	1.4	1.2	0.8	4.9	-	-
Concrete	10.0	14.7	8.2	14.5	8.5	16.0	8.0	25.1	1.73

wood, acrylic, PVC, and cardboard but higher than stainless steel. At 10°, the reported RL of drywall is 9.8 dB. For wood, PVC, and acrylic the measured reflection loss at 15° is also higher compared to 30°, but the difference is smaller than for drywall. The reflection loss of 6.5 to 8 dB for glass with incident angle 45° reported by Olsson et al. corresponds well to our measured reflection loss of 7.8 dB for vertical co-polarization, whereas the reported reflection loss for a wooden door is considerably higher than our measured reflection loss of wood and tabletop materials.

For materials acrylic, MDF wood, and the wooden tabletop, the measured reflection loss for cross-polarized antennas is within the noise floor of the channel sounder. For cardboard, the cross-polarized reflection loss is 37.4 dB, which is 17.1 dB higher than the co-polarized reflection loss. For PVC, the cross-polarized reflection loss is 38.0 dB and for stainless steel it is 19.6 dB. As the difference between the cross- and co-polarized reflection measurements is smaller than the antenna XPD for cardboard and stainless steel, we conclude that depolarization effects occur.

Table 5 also lists the results of the MMSE estimation of the refractive index. The fitted refractive index value for acrylic corresponds to the result we obtained from the penetration loss measurement and free spectral range. For PVC, there is a small difference of 0.13 between the two methodologies. Compared to an estimation of the refractive index based on time-domain spectroscopy, the fitted refractive index of wood is slightly higher than the reported value of 1.4, while the refractive index of glass is slightly lower than the reported value of 2.6 [26]. The index of refraction of PVC corresponds to the value of 1.6 that is reported in [28]. Given that a Fresnel curve does not provide an optimal fit to reflection coefficients above 100 GHz [34], the fitted refractive indices correspond well with previous research.

C. DIFFRACTION LOSS

Figure 8 visualizes measured diffraction loss as a function of frequency for the different TX-RX angle combinations and Fig. 9 shows the diffraction loss as a function of RX angle for fixed TX angle and a fixed frequency. The diffraction loss calculated via a knife-edge diffraction (KED) model is also shown. As the Fresnel diffraction parameter ν increases with frequency, the diffraction loss is also expected to increase with frequency, which does not correspond to
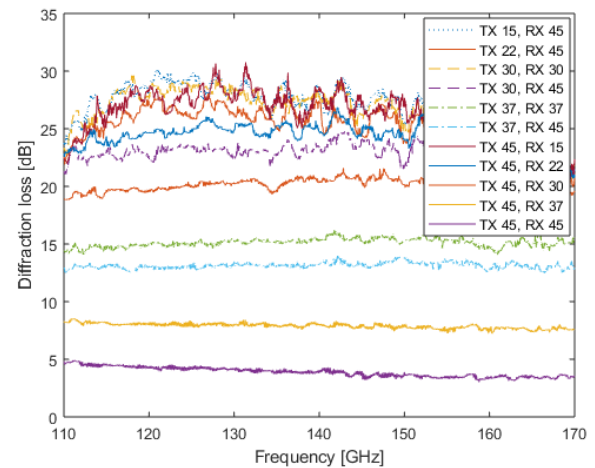
FIGURE 8. Averaged measured diffraction loss as a function of frequency for the different TX-RX angle combinations.
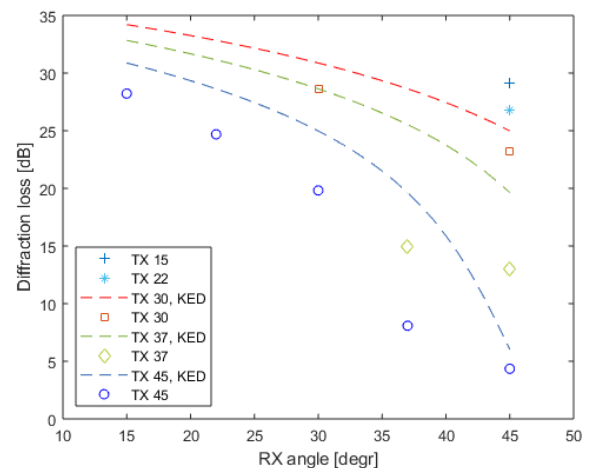
FIGURE 9. Averaged measured diffraction loss at 120 GHz as a function of RX angle for the different TX angles with a knife-edge model for TX angles 30°, 37° and 45°.

our measurements. For diffraction angles higher than 23° the signal-to-noise ratio (SNR) was too low. We expect the diffraction loss at both TX and RX angles 45°, i.e., diffraction angle 0°, to be 6 dB, whereas the measured loss is 5 dB. This can be caused by antenna misalignment, with the corner not exactly at the antenna's boresight. Compared to our
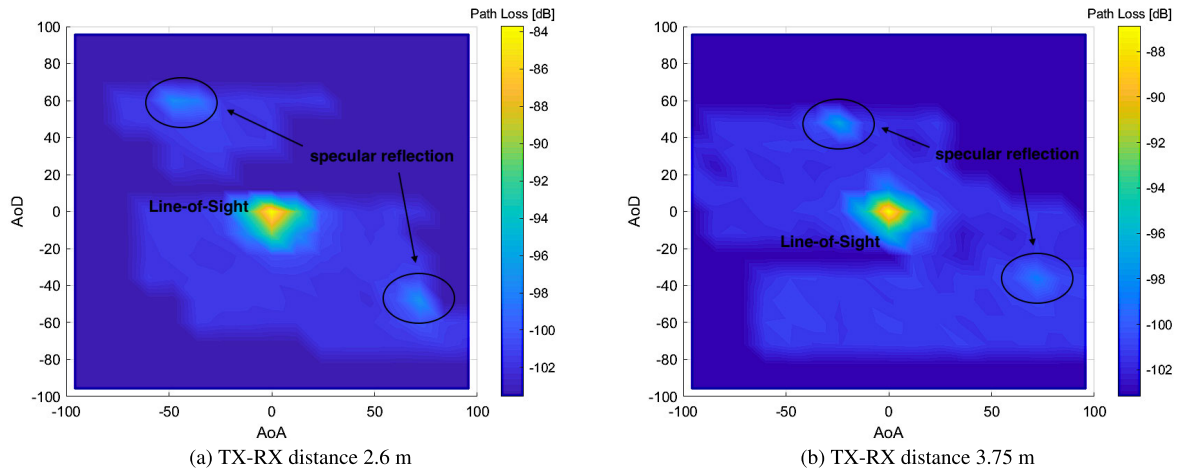
(a) TX-RX distance 2.6 m

(b) TX-RX distance 3.75 m

FIGURE 10. Power angular profile with path loss as a function of TX and RX angle, for two distances in a conference room.

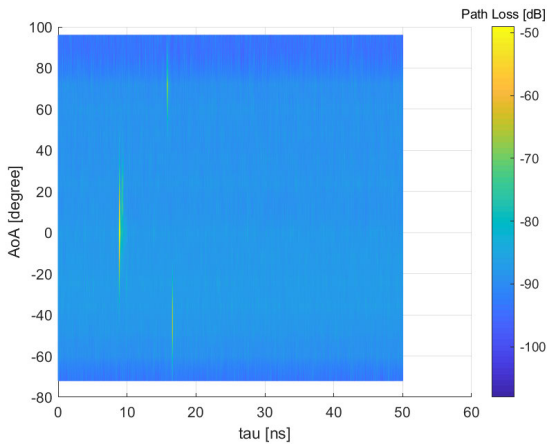**FIGURE 11.** Spatio-temporal model corresponding to distance 2.6 m.

TABLE 6. Characteristics multipath components.

Distance	Path	Path loss	Delay	AoA	AoD
	LOS	83.7 dB	8.9 ns	0°	0°
2.6 m	Refl 1	97.1 dB	15.9 ns	72°	-48°
	Refl 2	97.5 dB	16.6 ns	-48°	60°
	LOS	86.9 dB	12.7 ns	0°	0°
3.75 m	Refl 1	98.8 dB	19.9 ns	72°	-36°
	Refl 2	97.0 dB	16.5 ns	-24°	48°

measurements the KED model over-estimates diffraction loss with a difference up to 10 dB for TX and RX angles 37°. The over-estimation was also reported at lower frequencies (10 and 26 GHz) [18]. The lower diffraction loss was caused by penetration through the corner and multipath propagation. Both effects are negligible in our measurement setup, but due to the smaller wavelength, the corner cannot be modeled by a perfectly straight edge. Also, the KED model assumes the edge to be a sharp obstacle, at which a secondary electromagnetic source is defined according to the Huygens principle. The wavefront of this secondary source propagates in the geometric shadow area. However, the considered corner is not a sharp obstacle and due to the 90° concrete corner, no wavefront propagates in this region. It should also be noted that our measurement setup did not have millimeter-level accuracy, which explains the difference between different measurement runs.

D. SPATIO-TEMPORAL CONFERENCE ROOM CHANNEL MODEL

Figure 10 shows the PAP for the two considered distances in the conference room, using a 10 GHz bandwidth around

center frequency 140 GHz. The spatio-temporal model is shown in Fig. 11. As expected, there is a strong LOS component in both figures, with an AoA/AoD of 0°, PL corresponding to free space PL and a delay corresponding to the distance between the two nodes. Next to the LOS component, two wall reflections are present with a slightly higher delay and higher PL. Compared to lower frequency bands, the channel is extremely sparse with respect to multipath components. Table 6 summarizes the multipath components' characteristics. The measured PL of the reflected paths corresponds well to the calculated PL, taking into account the reflection loss values from Sect. III-B. For the distance of 2.6 m there are two NLOS paths. The second reflected path has a path length of 4.2 m to which a free space PL of 87.9 dB corresponds. Adding a 9.9 dB reflection loss on glass (for incident angle 30°) results in a total PL of 97.8 dB which is only 0.3 dB higher than the measured PL. Similarly, the reflected path length for LOS distance 3.75 m is 4.5 m which corresponds to a free space PL of 88.5 dB. Adding the 7.8 dB reflection loss on glass results in a total PL of 96.3 dB compared to the measured PL of 97.0 dB. For a distance of 2.6 m we obtain an angular RMS spread of 35.4° and a delay spread of 1.76 ns. For a distance of 3.75 m the angular RMS spread increases to 47.6° and the delay spread is 1.81 ns. Due to the sparsity of the channel, a threshold of -75 dBm was used to avoid that noise samples were influencing the calculation of delay spread.

Next to the specular reflected components with PL values around 97-98 dB, it is clear that there is some diffuse scattering and higher-order reflections with PL values around 100-101 dB, as can be seen from Fig. 11.
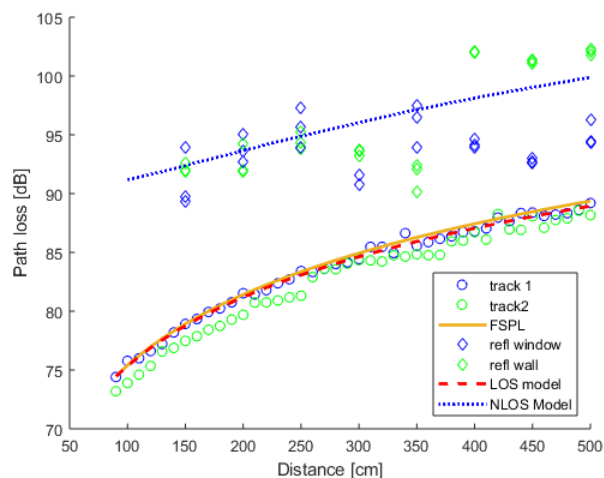
FIGURE 12. Outdoor path loss as a function of distance for frequency 140 GHz. Circles represent Line-of-Sight data from tracks 1 and 2 and diamonds represent reflected non-Line-of-Sight data. The fitted Line-of-Sight Floating-Intercept model is visualized by a dashed line, the non-Line-of-Sight Floating-Intercept model by a dotted line and free space path loss by a solid line.

E. OUTDOOR PATH LOSS MODEL

Figure 12 shows the measured PL as a function of distance for frequency 140 GHz for both LOS and NLOS measurements, as well as the fitted models. Theoretic FSPL at 1 m ranges from 73.3 dB at 110 GHz to 77.1 dB for 170 GHz. Fitting the LOS measurement data to a linear CI model results in a PL exponent ranging from 1.91 to 1.99 for all frequencies. A FI PL model, in which also the reference PL is fitted to the measurement data instead of being calculated via Friis formula, results in PL exponent values ranging from 1.92 to 1.98 and reference PL values that are within 0.3 dB from the free space PL values. For the NLOS measurement data, i.e., the reflected path via a window or wall reflection, the fitted reference PL of the FI model increases to 88.8 dB for 110 GHz, and up to 93.1 dB for 170 GHz, whereas the fitted PL exponent ranges from 0.9 to 1.5. The low PL exponent is caused by the specific geometry of the NLOS measurement, i.e., both TX and RX antennas are pointing towards a single reflection point on the building facade, and the RX antenna moves along a track that is parallel to the building. Because of the simple NLOS measurement setup, it is convenient to calculate PL as the sum of the propagation loss and a reflection loss. Indeed, the PL of the reflected path depends on the free space PL corresponding to distance d_{NLOS} as well as a reflection loss that depends on the incident angle θ, as can be seen in Fig. 4. With increasing distance, the incident angle increases and the reflection loss decreases. Due to the small distance to the building, the path length difference also decreases. Both effects contribute to a lower relative NLOS PL for higher distances compared to lower distances, which explains the low value of the fitted PL exponent. Therefore, the difference of attenuation between the LOS path and the reflected NLOS path decreases for larger distances, which can also be seen in Fig. 12. The root-mean-squared error between the measurements and the fitted

LOS model is 0.3 dB, which increases to 3.0 dB for the NLOS PL model.

IV. CONCLUSION AND FUTURE WORK

In this paper, material characteristics and radio channel models for D-band frequencies are presented. For the first time, the full 60 GHz bandwidth is characterized for distances up to 5 m, allowing measuring frequency selectivity. Measuring over the full band reveals that the thin film effect should be considered for both reflection and penetration when material thickness is in the order of 1 to 10 mm. Based on the periodicity and material thickness of the penetration loss measurements, refractive index values are obtained for acrylic and PVC. A second methodology for obtaining the refractive index at D-band frequencies is via an MMSE estimation based on the reflection coefficients. Both methods have similar results, which are in line with previous research using time-domain spectroscopy. Reflection loss depends on the polarization, i.e., whether the material is parallel or perpendicular to the field of incidence, whereas penetration loss does not depend on polarization. On the other hand, penetration loss increases with frequency, which is not the case for reflection loss. The highest measurable penetration loss was found for tabletop wood (50.5 dB), which shows a lower reflection loss. Materials with a higher reflection loss, such as acrylic and PVC, have a lower penetration loss. Diffraction loss around a concrete corner is measured for diffraction angles up to 20°, showing that a knife-edge diffraction model overestimates diffraction loss at D-band frequencies. Line-of-sight floating-intercept path loss models for a conference room and outdoors show a path loss close to free space. The conference room channel model includes a LOS component and first-order reflected components, from which the delay and amplitude correspond well to calculations based on the distance of the reflected path and the reflection loss. For the outdoor channel model, the additional attenuation of the reflected path is about 10 dB, so when there is a nearby reflector, the reflected path forms a fallback in case the LOS path is blocked.

Future work includes the implementation of the channel models in a ray tracer solution and implementing the unified channel model in a framework to automatically generate channel impulse response realizations.

REFERENCES
[1] T. S. Rappaport, G. R. Maccartney, M. K. Samimi, and S. Sun, ''Wideband millimeter-wave propagation measurements and channel models for future wireless communication system design,'' *IEEE Trans. Commun.*, vol. 63, no. 9, pp. 3029–3056, Sep. 2015.

[2] Y. Niu, Y. Li, D. Jin, L. Su, and A. V. Vasilakos, "A survey of millimeter wave communications (mmWave) for 5G: Opportunities and challenges," *Wireless Netw.*, vol. 21, no. 8, pp. 2657–2676, 2015, doi: 10.1007/s11276-015-0942-z.

[3] S. Hur, S. Baek, B. Kim, Y. Chang, A. F. Molisch, T. S. Rappaport, and K. Haneda, "Proposal on millimeter-wave channel modeling for 5G cellular system," *IEEE J. Sel. Topics Signal Process.*, vol. 10, no. 3, pp. 454–469, Apr. 2016.

[4] *Study on Channel Model for Frequencies From 0.5 to 100 GHz*, document (TR) 38.901, 3GPP, 2017.

[5] X. Zhao, S. Li, Q. Wang, M. Wang, S. Sun, and W. Hong, "Channel measurements, modeling, simulation and validation at 32 GHz in outdoor microcells for 5G radio systems," *IEEE Access*, vol. 5, pp. 1062–1072, 2017.

[6] X. Wu, C.-X. Wang, J. Sun, J. Huang, R. Feng, Y. Yang, and X. Ge, "60-GHz millimeter-wave channel measurements and modeling for indoor office environments," *IEEE Trans. Antennas Propag.*, vol. 65, no. 4, pp. 1912–1924, Apr. 2017.

[7] R. Sun, C. A. Gentile, J. Senic, P. Vouras, P. B. Papazian, N. T. Golmie, and K. A. Remley, "Millimeter-wave radio channels vs. synthetic beamwidth," *IEEE Commun. Mag.*, vol. 56, no. 12, pp. 53–59, Dec. 2018.

[8] C. De Lima, D. Belot, R. Berkvens, A. Bourdoux, D. Dardari, M. Guillaud, and M. Isomursu, "Convergent communication, sensing and localization in 6g systems: An overview of technologies, opportunities and challenges," *IEEE Access*, vol. 9, pp. 26902–26925, 2021.

[9] N. Rajatheva, I. Atzeni, E. Bicais, E. Bjornson, A. Bourdoux, and S. Buzzi, "Scoring the terabit/s goal: Broadband connectivity in 6G," 2021, *arXiv:2008.07220*.

[10] C.-L. Cheng, S. Kim, and A. Zajic, "Comparison of path loss models for indoor 30 GHz, 140 GHz, and 300 GHz channels," in *Proc. 11st Eur. Conf. Antennas Propag. (EUCAP)*, Mar. 2017, pp. 716–720.

[11] S. L. H. Nguyen, J. Järveläinen, A. Karttunen, K. Haneda, and J. Putkonen, "Comparing radio propagation channels between 28 and 140 GHz bands in a shopping mall," in *Proc. 12nd Eur. Conf. Antennas Propag.*, 2018, pp. 1–5.

[12] L. Pometcu and R. D'Errico, "Channel model characteristics in D-band for nlos indoor scenarios," in *Proc. 13rd Eur. Conf. Antennas Propag. (EuCAP)*, 2019, pp. 1–4.

[13] L. Pometcu and R. D'Errico, "An indoor channel model for high data-rate communications in D-band," *IEEE Access*, vol. 8, pp. 9420–9433, 2020.

[14] S. Kim, W. T. Khan, A. Zajić, and J. Papapolymerou, "D-band channel measurements and characterization for indoor applications," *IEEE Trans. Antennas Propag.*, vol. 63, no. 7, pp. 3198–3207, Jul. 2015.

[15] A. Al-Saman, M. Mohamed, M. Cheffena, and A. Moldsvor, "Wideband channel characterization for 6G networks in industrial environments," *Sensors*, vol. 21, no. 6, p. 2015, 2021. [Online]. Available: https://www.mdpi.com/1424-8220/21/6/2015

[16] D. Dupleich, R. Múller, S. Skoblikov, M. Landmann, G. D. Galdo, and R. Thoma, "Characterization of the propagation channel in conference room scenario at 190 GHz," in *Proc. 14th Eur. Conf. Antennas Propag. (EuCAP)*, Mar. 2020, pp. 1–5.

[17] A. K. M. Isa, A. Nix, and G. Hilton, "Impact of diffraction and attenuation for material characterisation in millimetre wave bands," in *Proc. Loughborough Antennas Propag. Conf. (LAPC)*, Nov. 2015, pp. 1–4.

[18] S. Deng, G. R. MacCartney, and T. S. Rappaport, "Indoor and outdoor 5G diffraction measurements and models at 10, 20, and 26 GHz," in *Proc. IEEE Global Commun. Conf. (GLOBECOM)*, Dec. 2016, pp. 1–7.

[19] G. L. Ramos, P. Kyosti, V. Hovinen, and M. Latva-aho, "Multiple-screen diffraction measurement at 10–18 GHz," *IEEE Antennas Wireless Propag. Lett.*, vol. 16, pp. 2002–2005, 2017.

[20] S. Hur, S. Baek, B. Kim, J. Park, A. F. Molisch, K. Haneda, and M. Peter, "28 GHz channel modeling using 3D ray-tracing in urban environments," in *Proc. 9th Eur. Conf. Antennas Propag. (EuCAP)*, 2015, pp. 1–5.

[21] S. Priebe, M. Kannicht, M. Jacob, and T. Kürner, "Ultra broadband indoor channel measurements and calibrated ray tracing propagation modeling at THz frequencies," *J. Commun. Netw.*, vol. 15, no. 6, pp. 547–558, 2013.

[22] C. Oestges, G. Hennaux, and Q. Gueuning, "Centimeter- and millimeter-wave channel modeling using ray-tracing for 5G communications," in *Proc. IEEE 82nd Veh. Technol. Conf. (VTC-Fall)*, Sep. 2015, pp. 1–5.

[23] J.-H. Lee, J.-S. Choi, J.-Y. Lee, and S.-C. Kim, "28 GHz millimeter-wave channel models in urban microcell environment using three-dimensional ray tracing," *IEEE Antennas Wireless Propag. Lett.*, vol. 17, no. 3, pp. 426–429, Mar. 2018.

[24] R. Charbonnier, C. Lai, T. Tenoux, D. Caudill, G. Gougeon, J. Senic, C. Gentile, Y. Corre, J. Chuang, and N. Golmie, "Calibration of ray-tracing with diffuse scattering against 28-GHz directional urban channel measurements," *IEEE Trans. Veh. Technol.*, vol. 69, no. 12, pp. 14264–14276, Jun. 2020.

[25] K. Guan, B. Peng, D. He, J. M. Eckhardt, H. Yi, S. Rey, B. Ai, Z. Zhong, and T. Kurner, "Channel sounding and ray tracing for intrawagon scenario at mmWave and sub-mmWave bands," *IEEE Trans. Antennas Propag.*, vol. 69, no. 2, pp. 1007–1019, Feb. 2021.

[26] R. Piesiewicz, T. Kleine-Ostmann, N. Krumbholz, D. Mittleman, M. Koch, and T. Kurner, "Terahertz characterisation of building materials," *Electron. Lett.*, vol. 41, no. 18, pp. 1002–1004, Sep. 2005.

[27] R. Piesiewicz, C. Jansen, D. Mittleman, T. Kleine-Ostmann, M. Koch, and T. Kürner, "Scattering analysis for the modeling of THz communication systems," *IEEE Trans. Antennas Propag.*, vol. 55, no. 11, pp. 3002–3009, Nov. 2007.

[28] R. Piesiewicz, C. Jansen, S. Wietzke, D. Mittleman, M. Koch, and T. Kürner, "Properties of building and plastic materials in the THz range," *Int. J. Infr. Millim. Waves*, vol. 28, no. 5, pp. 363–371, Mar. 2007.

[29] L. M. Correia and P. O. Frances, "Estimation of materials characteristics from power measurements at 60 GHz," in *Proc. 5th IEEE Int. Symp. Pers., Indoor Mobile Radio Commun., Wireless Netw. (PIMRC)*, vol. 2, Sep. 1994, pp. 510–513.

[30] T. S. Rappaport, Y. Xing, O. Kanhere, S. Ju, A. Madanayake, S. Mandal, A. Alkhateeb, and G. C. Trichopoulos, "Wireless communications and applications above 100 GHz: Opportunities and challenges for 6G and beyond," *IEEE Access*, vol. 7, pp. 78729–78757, 2019.

[31] C. R. Anderson and T. S. Rappaport, "In-building wideband partition loss measurements at 2.5 and 60 GHz," *IEEE Trans. Wireless Commun.*, vol. 3, no. 3, pp. 922–928, May 2004.

[32] J. Ryan, G. R. MacCartney, and T. S. Rappaport, "Indoor office wideband penetration loss measurements at 73 GHz," in *Proc. IEEE Int. Conf. Commun. Workshops*, Jan. 2017, pp. 228–233.

[33] M. Khatun, C. Guo, D. Matolak, and H. Mehrpouyan, "Indoor and outdoor penetration loss measurements at 73 and 81 GHz," in *Proc. IEEE Global Commun. Conf. (GLOBECOM)*, Dec. 2019, pp. 1–5.

[34] Y. Xing, O. Kanhere, S. Ju, T. S. Rappaport, and G. R. MacCartney, "Verification and calibration of antenna cross-polarization discrimination and penetration loss for millimeter wave communications," in *Proc. IEEE 88th Veh. Technol. Conf. (VTC-Fall)*, Aug. 2018, pp. 1–6.

[35] Y. Xing and T. S. Rappaport, "Propagation measurement system and approach at 140 GHz-moving to 6G and above 100 GHz," in *Proc. IEEE Global Commun. Conf. (GLOBECOM)*, Dec. 2018, pp. 1–6.

[36] Y. Xing, O. Kanhere, S. Ju, and T. S. Rappaport, "Indoor wireless channel properties at millimeter wave and sub-terahertz frequencies," in *Proc. IEEE Global Commun. Conf. (GLOBECOM)*, Dec. 2019, pp. 1–6.

[37] B.-E. Olsson, C. Larsson, M. N. Johansson, and S. L. H. Nguyen, "Radio propagation in an office environment at 140 GHz and 28 GHz," in *Proc. 15th Eur. Conf. Antennas Propag. (EuCAP)*, Mar. 2021, pp. 1–4.

[38] B. De Beelde, D. Plets, E. Tanghe, and W. Joseph, "Directional sub-THz antenna-channel modelling for indoor scenarios," in *Proc. 15th Eur. Conf. Antennas Propag. (EuCAP)*, Mar. 2021, pp. 1–4.

BRECHT DE BEELDE received the M.Sc. degree in electrical engineering from Ghent University, Belgium, in 2013, where he is currently pursuing the Ph.D. degree. He started his career as an Embedded SW Engineer at the Low-Power Wireless Division, Qorvo, Inc., where he worked on BLE and ZigBee communication controllers. He joined the WAVES Research Group, Department of Information Technology (INTEC), Ghent University/IMEC, in 2018. His research interests include channel modeling and wireless network planning in industrial environments and at mm-wave and sub-terahertz frequencies.

DAVID PLETS (Member, IEEE) received the M.Sc. degree in electrical engineering from Ghent University, Belgium, in 2006, and the Ph.D. degree, in 2011. He joined the WAVES Research Group, Ghent University/IMEC, in 2006. Since 2016, he has been an Assistant Professor. His current research interests include localization techniques and the IoT for both industry- and health-related applications. He is also involved in the optimization of wireless communication and broadcast networks, with a focus on coverage, exposure, and interference.

CLAUDE DESSET (Member, IEEE) has been a Senior Researcher with IMEC, Leuven, Belgium, since 2001. His main expertise is on high-throughput wireless communication systems and signal-processing, focusing on modeling and optimizing physical-layer performance and power consumption. He is especially targeting MIMO-OFDM systems and algorithms, error-correction coding, and the impact of hardware implementation constraints. He is investigating massive MIMO and mm-wave communication systems, but also emerging mm-wave radars.

EMMERIC TANGHE (Member, IEEE) received the M.Sc. degree in electrical engineering from Ghent University, Belgium, in July 2005, and the Ph.D. degree with a dissertation on the modeling of indoor and outdoor propagation through field measurements, in 2011. He joined the WAVES Research Group, Ghent University/IMEC, in 2005. He became a part-time Professor of medical applications of electromagnetic fields in and around the human body, in 2015. He continues his work on propagation modeling, covering indoor and outdoor propagation as well as propagation for wireless body area networks and medical implants.

ANDRÉ BOURDOUX (Senior Member, IEEE) received the M.Sc. degree in electrical engineering from the Université Catholique de Louvain, Belgium, in 1982. In 1998, he joined IMEC. He is currently a Principal Member of Technical Staff with the Advanced RF Research Group, IMEC. He is also a System Level and Signal Processing Expert for both the mm-wave wireless communications and radar teams. He has more than 15 years of research experience in radar systems and 15 years of research experience in broadband wireless communications. His research interests include advanced architectures, signal processing and machine learning for wireless physical layer, and high-resolution 3D/4D radars.

WOUT JOSEPH (Senior Member, IEEE) received the M.Sc. degree in electrical engineering from Ghent University, Belgium, in 2000, and the Ph.D. degree with a dissertation on measuring and modeling of electromagnetic fields around base stations in order to assess the health effects of the exposure to electromagnetic radiation, in 2005. He joined the WAVES Research Group, Ghent University/IMEC, in 2000. Since October 2009, he has been a Professor in the domain of experimental characterization of wireless communication systems. His research interests include electromagnetic field exposure assessment, in-body electromagnetic field modeling, electromagnetic medical applications, propagation for wireless communication systems, the IoT, and antennas and calibration. Furthermore, he specializes in wireless performance analysis and quality of experience.

• • •